On the origin of carrier localization in AlInAsSb digital alloy

Wen-Guang Zhou(周文广)[1,2], Dong-Wei Jiang(蒋洞微)[1,2], Xiang-Jun Shang(尚向军)[1,2], Dong-Hai Wu(吴东海)[1,2], Fa-Ran Chang(常发冉)[3], Jun-Kai Jiang(蒋俊锴)[1,2], Nong Li(李农)[1,2], Fang-Qi Lin(林芳祁)[1,2], Wei-Qiang Chen(陈伟强)[1,2], Hong-Yue Hao(郝宏玥)[1,2], Xue-Lu Liu(刘雪璐)[1,2], Ping-Heng Tan(谭平恒)[1,2], Guo-Wei Wang(王国伟)[1,2,†], Ying-Qiang Xu(徐应强)[1,2,‡], and Zhi-Chuan Niu(牛智川)[1,2,§]

[1] *State Key Laboratory for Superlattices and Microstructures, Institute of Semiconductors, Chinese Academy of Sciences, Beijing* 100083, *China*
[2] *College of Materials Science and Opto-Electronic Technology, University of Chinese Academy of Sciences, Beijing* 100049, *China*
[3] *School of Electronic Science and Engineering, Nanjing University, Nanjing* 210093, *China*

(Received 10 November 2022; revised manuscript received 21 April 2023; accepted manuscript online 24 April 2023)

We compared the photoluminescence (PL) properties of AlInAsSb digital alloy samples with different periods grown on GaSb (001) substrates by molecular beam epitaxy. Temperature-dependent S-shape behavior is observed and explained using a thermally activated redistribution model within a Gaussian distribution of localized states. There are two different mechanisms for the origin of the PL intensity quenching for the AlInAsSb digital alloy. The high-temperature activation energy E_1 is positively correlated with the interface thickness, whereas the low-temperature activation energy E_2 is negatively correlated with the interface thickness. A quantitative high-angle annular dark-field scanning transmission electron microscopy (HAADF-STEM) study shows that the interface quality improves as the interface thickness increases. Our results confirm that E_1 comes from carrier trapping at a state in the InSb interface layer, while E_2 originates from the exciton binding energy due to the roughness of the AlAs interface layer.

Keywords: photoluminescence spectroscopy, optical properties, AlInAsSb, digital alloy

PACS: 85.60.Gz, 68.65.Cd, 78.55.–m, 68.35.Ct **DOI:** 10.1088/1674-1056/accf7b

1. Introduction

The development of novel III–V quaternary alloys is gaining increasing attention in optoelectronic devices. Among these materials, $Al_xIn_{1-x}As_ySb_{1-y}$ (henceforth referred to as AlInAsSb) quaternary alloy is an attractive antimonide-based epi-structure because of its ability to tune the bandgap and band offset of heterostructures matched to the lattice of InP, InAs, or GaSb substrates.[1,2] This alloy appears to be better suited to light imaging, detection and ranging (LIDAR), and fiber-optic communications applications, where the avalanche photodiodes (APDs) serve as a key optical receiver.[3,4] In particular, several studies have demonstrated that AlInAsSb digital alloy APDs have comparable excess noise to Si APDs,[5] as well as direct bandgaps, high absorption coefficients, broader spectral response areas, and flexible structural designs.[6,7]

Despite these device achievements, the fundamental characteristics of the AlInAsSb material system are still largely unknown. Early research shows that the difficulty of growing AlInAsSb random alloy limits its applications. Due to its large and severe thermodynamic miscibility gap, AlInAsSb tends to segregate into inhomogeneous mixes of binary and ternary forms.[8,9] To resolve these issues, Scott Maddox *et al.*[10] recently adopted a "digital alloy" growth approach, a short-period superlattice, to build AlInAsSb inside the miscibility gap, employing a shutter sequence of AlSb, AlAs, AlSb, InSb, InAs, and InSb. To establish lattice matching with GaSb substrates, InSb and AlAs interface layers are employed. The quality of these interfaces, where carriers can scatter, has a significant impact on the performance of optoelectronic devices.[11] Therefore, evaluating the performance of AlInAsSb digital alloy devices requires a complete understanding of the quality of these interfaces.

The presence or absence of carrier localization in heterostructures is one sign of interface quality. Photoluminescence (PL) spectroscopy is a straightforward approach to evaluate localized states in heterogeneous systems.[12,13] In the presence of any localized state in heterogeneous, the PL peak emission energy will display S-[14] or V-shape[15] temperature dependency, which is contradictory with the behavior of a semiconductor band gap anticipated by the Varshni formula.[16] Carrier localization has been observed with PL in superlattices such as InAs/GaSb,[17] InAs/InAsSb,[18] InAs/AlSb,[12] and InAsSb/InSb.[19]

In this work, we employ temperature-dependent PL spectra to examine the impacts of interfaces in AlInAsSb digital alloy samples grown by molecular beam epitaxy for different periods. A temperature-dependent S-shape behavior is discovered, indicating the presence of localized states. In order to examine the probable origin and comprehend the mechanism

†Corresponding author. E-mail: wangguowei@semi.ac.cn
‡Corresponding author. E-mail: yingqxu@semi.ac.cn
§Corresponding author. E-mail: zcniu@semi.ac.cn

involved in the recombination process, the localized states and thermal activation energy are also investigated.

2. Experiments

The samples investigated in this study were grown by Veeco GenII molecular beam epitaxy (MBE) system on tellurium (Te) doped n-GaSb (001) substrate. The GaSb (5× to 3×) substrate reconstruction transition temperature of T_c = 540 °C was employed to calibrate the growth temperature. A 300-nm GaSb buffer layer was first grown at 630 °C to smooth the surface. The $Al_{0.7}In_{0.3}AsSb$ digital alloy was subsequently grown at 540 °C and had a nominal digital alloy period thickness of 10 monolayers (ML) or 3.05 nm. The total thickness of AlInAsSb digital alloy is around 300 nm with 99 periods. A symmetric 15-nm AlSb barrier aided PL studies by restricting the photogenerated carriers to the AlInAsSb digital alloy layer. The comprehensive experimental details have been reported in our previous report.[20] Two samples with InSb thicknesses of 0.1 ML ×2 (sample A) and 0.4 ML ×2 (sample B) were investigated in the work. The thickness of the remaining binary alloy changes with the thickness of the InSb layer, such that the films are lattice-matched to the GaSb substrate, whereas the total AlSb and AlAs thickness is 7 ML. The period information of these two $Al_{0.7}In_{0.3}AsSb$ digital alloys is shown in Fig. 1.

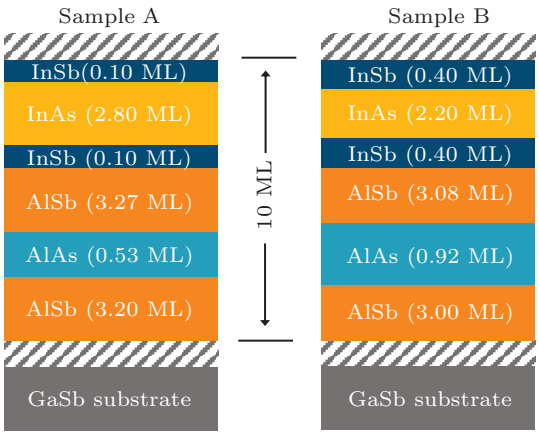

Fig. 1. Period information of two $Al_{0.7}In_{0.3}AsSb$ digital alloys.

The material quality of the two samples was assessed using high-resolution x-ray diffraction (HRXRD) and atomic force microscopy (AFM). For PL measurements, the pump laser was a 532-nm solid-state laser with 250 mW of power focused on a 150-μm diameter spot. The signal was detected using a spectrometer equipped with a liquid nitrogen-cooled InGaAs detector. For the temperature-dependent measurements, the samples were mounted on the cold finger of a closed-cycle helium cryostat. The measurements were taken at various temperatures, from 10 K to 300 K. High-angle annular dark-field scanning transmission electron microscopy (HAADF-STEM) experiments were performed on an aberration-corrected JEOL JEM-ARM200F microscope operated at 200-kV acceleration voltage equipped with a Gatan GIF Quantum ER spectrometer.

3. Results and discussion

3.1. Structural analysis

Figures 2(a) and 2(b) represent the 2θ–ω scans of samples A and B, respectively. The mismatch between the zero-order satellite peak of sample A and the GaSb substrate is ~ -1092 ppm, while sample B exhibits a mismatch of ~ -993 ppm, suggesting that both samples are lattice-matched to the substrate. The digital alloy period of the two samples is determined to be 29.82 Å and 30.47 Å from the spacings between the satellites, which agrees with our design (30.48 Å). The appearance of various satellite peaks indicates the high crystal quality of the AlInAsSb digital alloy. The full width at half-maximum (FWHM) of the first-order satellite peak is 55.85 arcsec for sample A and 48.5 arcsec for sample B, indicating an increase in the thickness of the interface and an improvement in the crystalline quality of the material. The atomic steps can be clearly seen in the AFM results shown in the insets of Figs. 2(a) and 2(b). The small root-mean-square (RMS) roughness of 1.967 Å and 2.052 Å, respectively, over 10 μm×10 μm area.

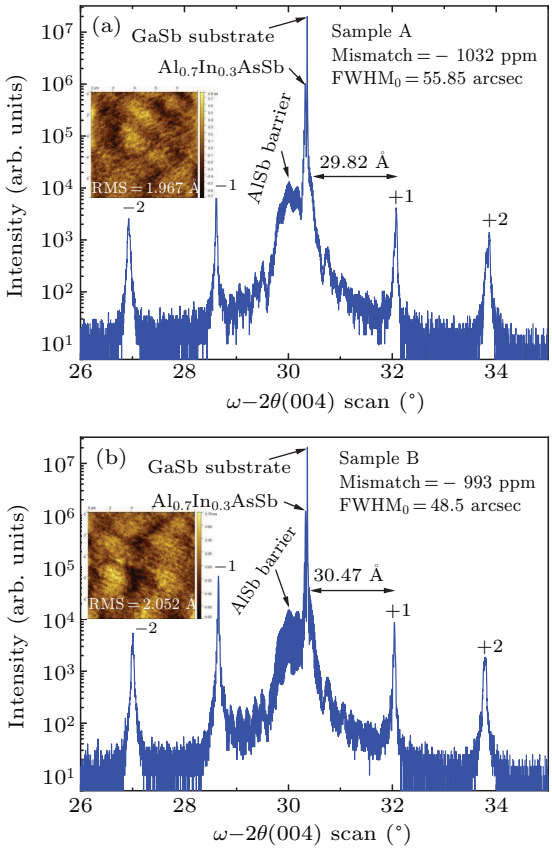

Fig. 2. HRXRD 2θ–ω rocking scans for (a) sample A and (b) sample B in the vicinity of GaSb (004) reflection. The inset shows AFM image of the sample surface over 10 μm×10 μm area.

3.2. Optical investigation

The temperature-dependent PL spectra of samples A and B are shown in Figs. 3(a) and 3(b), respectively. As shown in the PL spectra, the peak position of both samples displays a redshift-blueshift-redshift pattern (S-shape behavior), which is not consistent with the behavior of a semiconductor band gap anticipated by the Varshni[16] or Bose–Einstein[21] formulae. Previous observations of this effect in various material systems[14,22–25] have been attributed to the carrier localization effect caused by the electric potential fluctuation due to crystal defects, interface roughness, and band offsets between the constituent layer and interfacial layer. Notably, a weak peak at around 948 nm in the PL spectra of both samples, the peak position of which does not vary with temperature and becomes more pronounced with increasing temperature. The PL intensity decreases with increasing temperature due to non-radiative recombination processes, making the weak peak more pronounced at high temperatures. Therefore, this weak peak is identified as a noise peak that is introduced by the test equipment or by the test process.

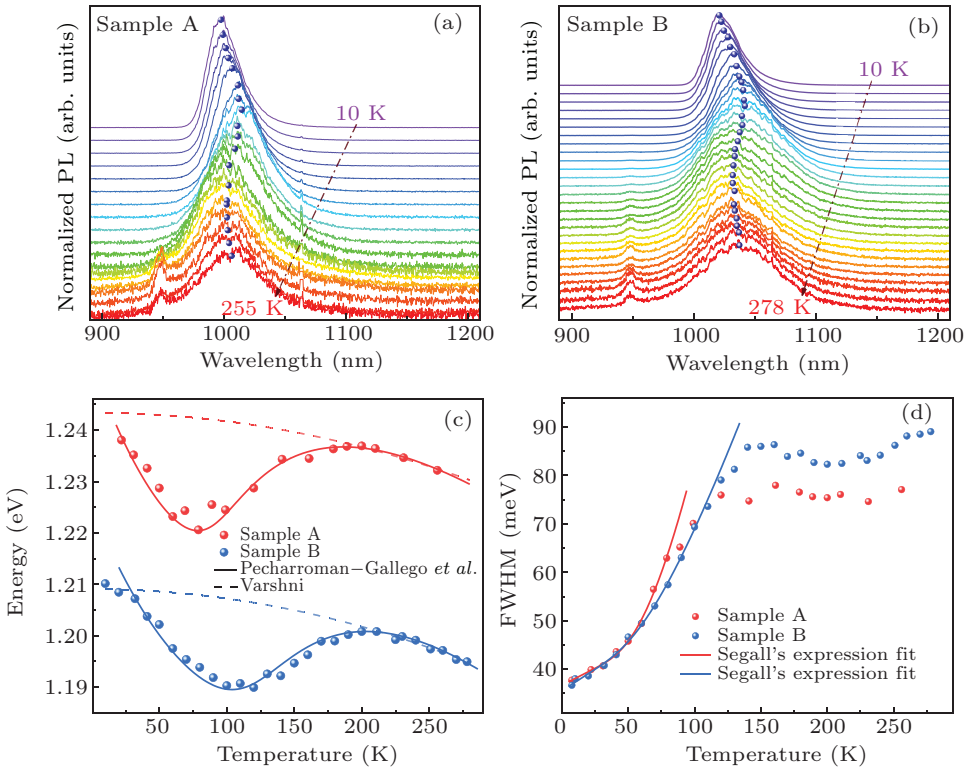

Fig. 3. Temperature-dependent PL spectra of (a) sample A and (b) sample B (data scaled for clarity). (c) PL emission peak energy of samples A and B as a function of temperature. (d) Variation in FWHM with temperature for sample A and sample B. Experimental data (solid circles) are fitted to Eq. (1) and Segall's equation (solid lines).

To illustrate this S-shaped behavior, we show the variation in E_{PL}, the PL peak emission energy, with temperature for both samples in Fig. 3(c). The E_{PL} was extracted by Gaussian fitting. A quantitative theoretical model has been employed to investigate the E_{PL} with temperature, and it was utilized before by Pecharroman–Gallego *et al.*[24] The model is a conjugation of the localized state ensemble (LSE) model[26] provided by Li *et al.*,[27] which considers thermally activated redistribution within a Gaussian (energy) distribution of localized states, and the empirical function proposed by O'Donnell and Chen.[28] The empirical function is used to fit the bandgap shrinking behavior of semiconductors with room-temperature gaps between 1.0 eV and 5.5 eV. O'Donnell and Chen demonstrated the applicability of the function based on electron–hole pairs creation. The E_{PL} is given by the expression

$$E_{\mathrm{PL}} = E_{\mathrm{PL}}(0) - S\langle E_{\mathrm{ph}}\rangle\left[\coth\left(\frac{\langle E_{\mathrm{ph}}\rangle}{2K_{\mathrm{B}}T}\right)-1\right] - x(T)K_{\mathrm{B}}T, \tag{1}$$

where K_{B} is Boltzmann's constant, $E_{\mathrm{PL}}(0)$ is the emission peak energy at 0 K, S is related to the Huang–Rhys parameter, a dimensionless coupling constant that represents the strength with which the radiative transition couples with the LO polarization field,[29] $\langle E_{\mathrm{ph}}\rangle$ is the average phonon energy and $x(T)$ is a dimensionless coefficient that can be obtained by numerically solving the equation[23]

$$x\mathrm{e}^{x} = (\tau_{\mathrm{r}})\left[\left(\frac{\sigma}{K_{\mathrm{B}}T}\right)^{2} - x\mathrm{e}^{(E_0-E_{\mathrm{a}})/K_{\mathrm{B}}T}\right], \tag{2}$$

where τ_{r} represents the ratio of the carrier recombination time

to the carrier transfer time, $E_a - E_0$ is the barrier height that carriers must overcome to transfer and represents an averaged value of the depth of localization, and σ is the width of the Gaussian distribution of localized states, which describes the broadening of the absorption edge. The results of fitting Eq. (1) displayed as solid curves in Fig. 3(c) correlate well with the experimental data for both samples, demonstrating that the theoretical and experimental results correspond well.

Table 1. Fitted parameters of the emission peak energy obtained from Eqs. (1) and (2).

	E_0 (eV)	S	$E_a - E_0$ (meV)	τ_r	σ (meV)
Sample A	1.2741	1.47005	20	600	21.11
Sample B	1.2603	1.92412	34	220	27.67

The extracted fitted parameters for samples A and B are shown in Table 1, where $\langle E_{ph} \rangle$ fixed for 42.1 meV using Raman characterization. The Raman spectra of both samples are shown in Fig. S1 of the supporting information. It should be noted from Fig. S1 that the observed spectral bands are almost identically positioned between the two samples. The larger the value of the depth of localization ($E_a - E_0$), the more difficult it is for carriers to escape to level E_a. Sample A exhibits a lower $E_a - E_0$ than sample B, showing that increasing the thickness of the InSb and AlAs layers enhances the localization depth. The broadening parameter σ increases with the thickness of the InSb and AlAs layers, indicating that the distribution width of the localized states is subject to an increase with interface thickness. As can be noticed, sample B has a greater electron–phonon coupling constant S than sample A. This shows that sample B has a greater lattice relaxation of the excited state due to increased electron–phonon coupling.

Furthermore, figure 3(d) shows the temperature dependency of the FWHM for samples A and B. The FWHM displays an inverted S-shaped behavior in both samples, which confirms the presence of a competing process between the recombination of local excitons and free excitons. The FWHM peaks can be utilized to determine the temperature at which the rivalry between localized and free excitons is greatest.[30] In our case, the FWHM maxima occur at 130 K and 150 K for samples A and B, respectively. This is consistent with the increase in interface thickness in both samples. Additionally, we discovered that the FWHMs of the two samples overlap at approximately 110 K. As a result, Segall's equation[31] was used to fit both sample A (10 K–80 K) and sample B (10 K–100 K)

$$\Gamma(T) = \Gamma_0 + \Gamma_{ac} T + \frac{\Gamma_{op}}{e^{\hbar\omega/(K_B T)} - 1},$$

where Γ_0, Γ_{ac}, and Γ_{op} are the inhomogeneous broadening, the exciton–acoustic phonon interaction, and the exciton–optical phonon influence on the peak width broadening, respectively. The optical phonon energy $\hbar\omega$ of sample B (20.69 meV) is smaller than that of sample A (22.86 meV), indicating the better crystalline and optical quality of sample B. At low temperatures, this means that sample B has a smaller FWHM than sample A. When raising the temperature over 80 K, the local carriers of sample A transform into free carriers, while the carriers are still trapped in the greater depth of localization of sample B. Carrier redistribution leads to the FWHM increasing at a lower rate or even decreasing slightly, so that both samples have the same FWHM at approximately 110 K.

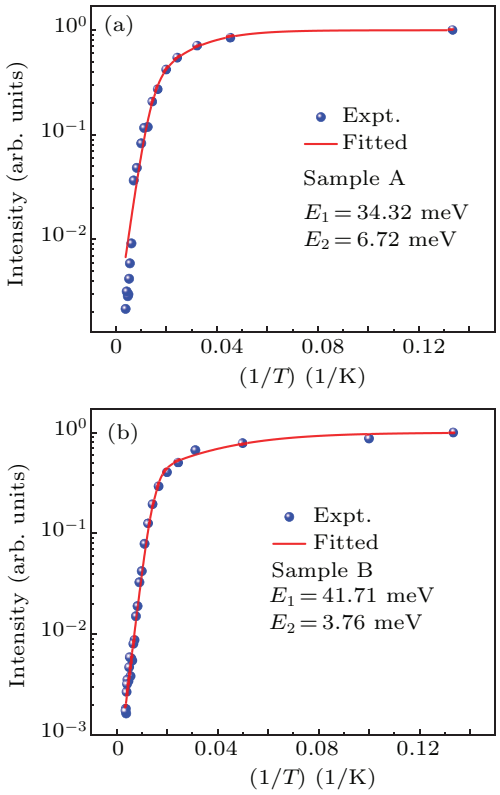

Fig. 4. Integrated PL intensity variation with reciprocal temperature was used to calculate the activation energy for (a) sample A and (b) sample B. The red lines indicate the fitting lines achieved by Eq. (3).

Figure 4 shows the normalized integrated PL intensity as a function of reciprocal temperature for both samples. To further understand the influences of the interface on the recombination processes in AlInAsSb digital alloy, the activation energy in the thermally activated process is calculated with the following formula:[32,33]

$$I(T) = \frac{I_0}{1 + \sum_{i=1}^{n} A_i \exp(-E_i/K_B T)}, \tag{3}$$

where I_0 is a constant, E_i is the activation energy for the nonradiative channel, and A_i is the dimensionless coefficient defined simply as the carrier capture time and carrier escape time of the nonradiative process. The best match to the experimental data was achieved for two localized states (two activation energies) in both samples. For sample A (B) $E_2 = 6.72$ meV (3.76 meV) is the thermal activation energy responsible for the low-temperature range of 10 K–80 K (10 K–105 K), and

$E_1 = 34.32$ meV (41.71 meV) is the thermal activation energy for the high-temperature range of 80 K–255 K (105 K–278 K).

The low-temperature activation energy E_2 is negatively correlated with the interface thickness, whereas the high-temperature activation energy E_1 is positively correlated with the interface thickness, indicating the presence of two nonradiative recombination centers in the interfacial layer. The low-temperature activation energy E_2 is likely to originate from a local state associated with the roughness of the interface as the E_2 values (6.72 meV and 3.76 meV) for both samples are comparable to the exciton binding energy in several quantum structure systems.[12,34,35] Figure 2 reveals that sample B has better crystal quality, suggesting that increasing the thickness of the interfacial layer generates a more uniform interface and reduces interfacial roughness. Furthermore, InSb-like interfaces have been proven to exhibit smoother interfacial and fewer point defects than AlAs-like interfaces in InAs/AlSb quantum wells and superlattices.[10,36] Hence, we can expect to observe the localized states originating from the exciton binding energy due to the rough AlAs-like interface.

The high-temperature activation energy E_1 is not compatible with the expected results for the Anderson localization.[37,38] In addition to Anderson localization, there is another possible explanation for carrier localization, Carrier trapping. Carrier trapping is caused by the energy state at the interfacial layer between two constituent layers in a superlattice material.[32] Therefore, E_1 likely arises from carrier trapping in energy states associated with the InSb-like interface. The photogenerated carriers are trapped in the energy states created by the InSb hole well, which are decoupled from the valence band of AlInAsSb digital alloy.[12] Indeed, this energy state at the InSb-like interface is known as the Tamm state.[39,40] According to the calculation result of Shen *et al.*,[41] the value of the Tamm state is proportional to the thickness of the InSb-like interface. The extracted E_1 of both samples is comparable to the 40-meV conclusion. When considering the increased thickness of the InSb-like interface due to 3s Sb soaking during the growth of the digital alloy, the value of E_1 is possible.

To further clarify the physical origin of low-temperature local states, the anion/cation column intensity profiles extracted from HAADF–STEM images were used to determine the interfacial roughness. The intensities of the atom columns in the HAADF–STEM images (Figs. 5(a) and 5(b)) are digitally processed using CalAtom software. The algorithm details have been described in the corresponding reference.[42] Figures 5(c) and 5(d) show the average intensities along with the standard deviation of these columns for samples A and B, respectively. Due to the different atomic numbers Z, the digital alloy region could be distinguished by the intensity ratio profiles, in line with the expectation. As it can be noted, the average intensity of the AlSb regions in sample B is relatively flat and has good homogeneity, which indicates a smoother interface in sample B. As a result, the interface quality improves with increasing interface thickness. The origin of the local state at low temperatures could be this interface roughness.

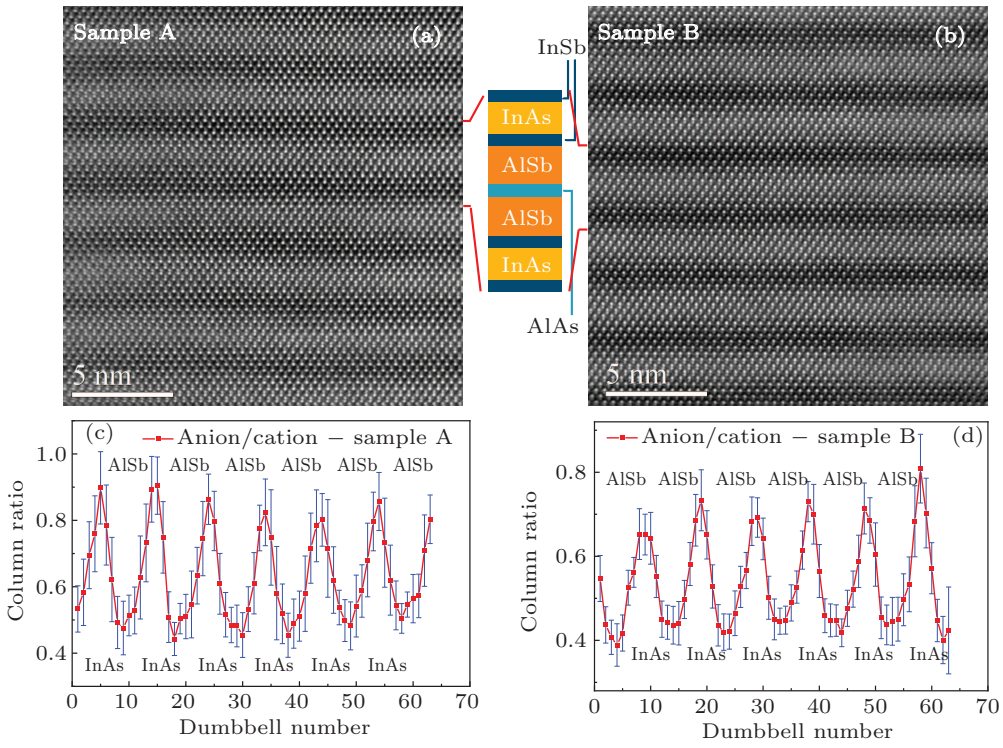

Fig. 5. Filtered HAADF–STEM images of (a) sample A and (b) sample B with the anion/cation intensity ratio profiles generated by CalAtom. The error bars in the plot show one standard deviation.

4. Conclusion

In summary, we compared the PL properties of AlInAsSb digital alloy samples with different periods. A thermally activated redistribution model was well fitted to the temperature-dependent "S-shaped" behavior. These results indicate that the localized state is more dominant in thicker interface layers. Two thermal activation energies were extracted by fitting the temperature dependence of the integrated PL intensities. The results demonstrate that the low-temperature activation energy originates from the AlAs-like interface roughness, whereas the high-temperature activation energy originates from the InSb-like interface state (Tamm state). Our findings suggest that increasing the interfacial thickness improves the crystalline quality of the material but introduces an interfacial state. Therefore, a trade-off must be considered when designing AlInAsSb digital alloy-based optoelectronic devices between the improvement in crystal quality and the effect of the local state on carrier transport.

Acknowledgements

The authors thank Professor Yuan Yao (the Institute of Physics, Chinese Academy of Sciences) for his help in HAADF–STEM testing and analysis.

Project supported by the National Key Technologies Research and Development Program of China (Grant Nos. 2019YFA0705203, 2019YFA070104, 2018YFA0209102, and 2018YFA0209104), the Major Program of the National Natural Science Foundation of China (Grant Nos. 61790581, 62004189, and 61274013), the Aeronautical Science Foundation of China (Grant No. 20182436004), the Key Research Program of the Chinese Academy of Sciences (Grant No. XDPB22), and the Research Foundation for Advanced Talents of the Chinese Academy of Sciences (Grant No. E27RBB03).

References

[1] Rojas-Ramirez J.S, Wang S, Contreras-Guerrero R, Caro M, Bhatnagar K, Holland M, Oxland R, Doornbos G, Passlack M, Diaz C H and Droopad R 2015 *J. Cryst. Growth* **425** 33
[2] Tournet J, Rouillard Y and Tournié E 2017 *J. Cryst. Growth* **477** 72
[3] Xie J, Zhang Z, Huang M, Li J, Jia F and Zhao Y 2022 *Chin. Phys. B* **31** 090701
[4] Campbell J C 2022 *IEEE J. Sel. Top. Quantum Electron.* **28** 3800911
[5] Woodson M E, Ren M, Maddox S J, Chen Y J, Bank S R and Campbell J C 2016 *Appl. Phys. Lett.* **108** 081102
[6] Ren M, Maddox S J, Woodson M E, Chen Y J, Bank S R and Campbell J C 2017 *J. Light. Technol.* **35** 2380
[7] March S D, Jones A H, Campbell J C and Bank S R 2021 *Nat. Photon.* **15** 468
[8] Vaughn L G 2006 *Mid-infrared multiple quantum well lasers using digitally-grown aluminum indium arsenic antimonide barriers and strained indium arsenic antimonide wells*, Ph. D. Dissertation (New Mexico: The University of New Mexico)
[9] Lyu Y X, Han X, Sun Y Y, Jiang Z, Guo C Y, Xiang W, Dong Y N, Cui J, Yao Y, Jiang D W, Wang G W, Xu Y Q and Niu Z C 2018 *J. Cryst. Growth* **482** 70
[10] Maddox S J, March S D and Bank S R 2016 *Cryst. Growth Des.* **16** 3582
[11] Yuan Y, Rockwell A K, Peng Y W, Zheng J Y, March S D, Jones A H, Ren M, Bank S R and Campbell J C 2019 *J. Light. Technol.* **37** 3647
[12] Lee S, Jo H J, Mathews S, Simon J A, Ronningen T J, Kodati S H, Fink D R, Kim J S, Winslow M, Grein C H, Jones A H, Campbell J C and Krishna S 2019 *Appl. Phys. Lett.* **115** 211601
[13] Li R, Xu M S, Wang P, Wang C X, Qu S D, Shi K J, Wei Y H, Xu X G and Ji Z W 2021 *Chin. Phys. B* **30** 047801
[14] Nuytten T, Hayne M, Bansal B, Liu H Y, Hopkinson M and Moshchalkov V V 2011 *Phys. Rev. B* **84** 045302
[15] Steenbergen E H, Massengale J A, Ariyawansa G and Zhang Y H 2016 *J. Lumin.* **178** 451
[16] Varshni Y P 1967 *Physica* **34** 149
[17] Bertru N, Baranov A N, Cuminal Y, Boissier G, Alibert C, Joullie A and Lambert B 1999 *J. Appl. Phys.* **85** 1989
[18] Lin Z Y, Liu S, Steenbergen E H and Zhang Y H 2015 *Appl. Phys. Lett.* **107** 201107
[19] Pepper B, Soibel A, Ting D, Hill C, Khoshakhlagh A, Fisher A, Keo S and Gunapala S 2019 *Infrared Phys. Technol.* **99** 64
[20] Chang F R, Hao R T, Qi T T, Zhao Q C, Liu X X, Li Y, Gu K, Guo J, Wang G W, Xu Y Q and Niu Z C 2019 *Chin. Phys. B* **28** 028503
[21] Viña L, Logothetidis S and Cardona M 1984 *Phys. Rev. B* **30** 1979
[22] Cho Y H, Gainer G H, Fischer A J, Song J J, Keller S, Mishra U K and DenBaars S P 1998 *Appl. Phys. Lett.* **73** 1370
[23] Li Q, Xu S J, Cheng W C, Xie M H, Tong S Y, Che C M and Yang H 2001 *Appl. Phys. Lett.* **79** 1810
[24] Pecharromán-Gallego R, Martin R W and Watson I M 2004 *J. Phys. Appl. Phys.* **37** 2954
[25] Maros A, Faleev N N, Bertoni M I, Honsberg C B and King R R 2016 *J. Appl. Phys.* **120** 183104
[26] Yu J J, Zhao Y N, Li S Q, Yao J S, Yao L, Ning J Q, Jiang Y C, Lu H, Chen B L and Zheng C C 2022 *J. Lumin.* **249** 119009
[27] Li Q, Xu S J, Xie M H and Tong S Y 2005 *Europhys. Lett.* **71** 994
[28] O'Donnell K P and Chen X 1991 *Appl. Phys. Lett.* **58** 2924
[29] Hopfield J J 1959 *J. Phys. Chem. Solids* **10** 110
[30] Lourenço S A, Dias I F L, Duarte J L, Laureto E, Aquino V M and Harmand J C 2007 *Braz. J. Phys.* **37** 1212
[31] Rudin S, Reinecke T L and Segall B 1990 *Phys. Rev. B* **42** 11218
[32] Xing J L, Zhang Y, Liao Y P, Wang J, Xiang W, Hao H Y, Xu Y Q and Niu Z C 2014 *J. Appl. Phys.* **116** 123107
[33] Hugues M, Damilano B, Duboz J Y and Massies J 2007 *Phys. Rev. B* **75** 115337
[34] Thoma J, Liang B L, Lewis L, Hegarty S P, Huyet G and Huffaker D L 2013 *Appl. Phys. Lett.* **102** 053110
[35] Georgiev N and Mozume T 2001 *J. Appl. Phys.* **89** 1064
[36] Tuttle G, Kroemer H and English J H 1990 *J. Appl. Phys.* **67** 3032
[37] Anderson P W 1958 *Phys. Rev.* **109** 1492
[38] Holthaus M, Ristow G H and Hone D W 1995 *Phys. Rev. Lett.* **75** 3914
[39] Kroemer H 1992 *J. Vac. Sci. Technol. B Microelectron. Nanometer Struct.* **10** 1769
[40] Shaw M J 1998 *J. Vac. Sci. Technol. B Microelectron. Nanometer Struct.* **16** 1794
[41] Shen J, Goronkin H, Dow J D and Ren S Y 1995 *J. Appl. Phys.* **77** 1576
[42] Zhang Q, Zhang L Y, Jin C H, Wang Y M and Lin F 2019 *Ultramicroscopy* **202** 114